Astron. Astrophys. 334, 805–813 (1998)

ASTRONOMY AND ASTROPHYSICS

A simple kinematic modeling for flattened S0 galaxies⋆

E. Loyer[1], **F. Simien**[2], **R. Michard**[3], **and Ph. Prugniel**[2]

[1] École Normale Supérieure de Lyon, 46 allée d'Italie, F-69364 Lyon Cedex 07, France
[2] CRAL-Observatoire de Lyon (CNRS: UMR 142), F-69561 St-Genis-Laval Cedex, France
[3] Observatoire de la Côte d'Azur, B.P. 139, F-06003 Nice Cedex 4, France

Received 26 January 1998 / Accepted 11 March 1998

Abstract. We present mass models for three S0 galaxies with a strong disk component observed almost on edge (NGC 2732, NGC 4111, and NGC 4350). For the analytical representation of the surface-brightness distribution, the method of Multi-Gaussian Expansion, first presented by Monnet et al. (1992: A&A 253, 366) is applied to V-band surface photometry. A simplified dynamical model is adopted, and the calculated kinematic profiles are compared to long-slit spectroscopic data; overall agreement is reached, except for the innermost region, where additional mass is needed for all three galaxies. We discuss possible applications.

Key words: galaxies: elliptical and lenticular, cD – galaxies: kinematics and dynamics – galaxies: fundamental parameters – galaxies: individual: NGC 2732 – galaxies: individual: NGC 4111 – galaxies: individual: NGC 4350

1. Introduction

It is well-known that, among early-type galaxies, S0s present a special interest. So far, most of the work on these objects has been devoted to surface photometry and stellar populations, but the interest of kinematics and dynamics is second to none: at stake may be valuable information on their formation and evolution processes. For this, highly flattened S0s present a decisive advantage: the visibility of a thin disk drastically reduces the uncertainty on their inclination with respect to the line of sight. Moreover, many of them have, as ellipticals, a very low content of dust, which limits the uncertainty inherent in the conversion of luminosity to mass. Modeling the global kinematics provided by long-slit spectroscopy has been unfrequent, however, and NGC 3115 (Capaccioli et al. 1993) is one of the very few examples of such a study.

One of the reasons for this situation may be the more complex luminosity distribution in flattened S0s with respect to elliptical galaxies. Many ellipticals can easily be represented by analytic luminosity laws (e.g. the $r^{1/n}$ function of Sérsic 1968) or, for more accuracy, can be processed by inversion algorithms (Lucy 1974). For edge-on S0s, the conspicuous two-component structure has focused most attention on a bulge+disk approximation (Capaccioli et al. 1987; Scorza & Bender 1990, 1995; Simien & Michard 1990). However, this physically meaningful representation of the surface-brightness distribution necessarily involves somewhat uncertain assumptions, and the technique can be rather tedious to implement.

Here, we study three edge-on S0 galaxies with a prominent disk. For a precise analytical representation of the luminosity distribution, we make use of the Multi-Gaussian Expansion (hereafter MGE); this method was presented by Monnet et al. (1992) and Emsellem et al. (1994a), and its ability to fit superimposed components with totally different geometries has already been tested on the inner region of M104 (Emsellem et al. 1994b, 1996). Our aim is to determine the global mass distribution from this 3D luminosity representation, with the help of a simplified dynamical model: its predictions are compared to the observational rotation-velocity and velocity-dispersion profiles as available from "classical" reductions. For this purpose, we solve the well-known second-order Jeans equations, taking advantage of the convenient properties of the MGE formalism, and we calculate the line-of-sight velocity distributions (LOSVDs); then, these LOSVDs are handled in a way similar to the actual observational process (in terms of seeing effects, rebinning, and reduction), so that a significant comparison is obtained between the model and the measurements.

The paper is organized as follows: Sect. 2 lists the main characteristics of the three galaxies, and presents all the data used subsequently (surface photometry and long-slit spectroscopy); Sect. 3 explains the application of the MGE method to the surface photometry; Sect. 4 presents the adopted dynamical model and the fitting to the spectroscopic data. A discussion of the results (Sect. 5) is followed by a short conclusion (Sect. 6).

2. The data

2.1. Selection

We have selected three highly-flattened objects, with the following criteria: a) evidence for an edge-on or nearly edge-on observation, so that the uncertainty on the actual angle has little influence on the component separation and on the kinematic

Send offprint requests to: F. Simien, (simien@obs.univ-lyon1.fr)

⋆ Based in part on observations collected at the Observatoire de Haute-Provence.

Table 1. Catalog elements for program galaxies

Object	T	$B_{\rm T}$	Δ	M_B	D_{25}	ϵ_{25}
(1)	(2)	(3)	(4)	(5)	(6)	(7)
NGC 2732	-2	12.85	28.8	-19.88	2.1	0.56
NGC 4111	-1	11.45	13.0	-19.38	4.6	0.78
NGC 4350	-2	11.90	17.4	-19.56	2.9	0.48

Notes. All columns, except col. (2), are from the LEDA database (status: LEDA1996). Col. (2): T, coded morphological type (RC3: de Vaucouleurs et al. 1991); col. (3): $B_{\rm T}$, integrated blue magnitude; col. (4): Δ, distance in Mpc, from heliocentric radial velocity, corrected for Virgocentric infall, and with $H_0 = 75\,{\rm km\,s^{-1}\,Mpc^{-1}}$; col. (5): M_B, absolute B luminosity; col. (6): D_{25}, isophotal diameter at $\mu_B = 25$ mag arcsec^{-2}, in arcmin; col. (7): ϵ_{25}, ellipticity at $\mu_B = 25$.

projection; b) availability of deep long-slit spectra, along (at least) the major axis; and c) availability of surface photometry in a pass-band close to that of the spectroscopy, for line-of-sight model integration consistent with the kinematic data. NGC 2732, NGC 4111, and NGC 4350 turned out to be satisfactory candidates; catalog elements are presented in Table 1.

2.2. Surface photometry

Our V-band data were secured at the CCD camera attached to the 1.20-m, $f/6$ telescope of the Observatoire de Haute-Provence. For NGC 4111 and NGC 4350, observed by J. Marchal and one of us (RM), the receptor was a RCA3 with 512×320 pixels of $0.83''$; the seeing FWHM was respectively 2.0 and $2.3''$. For NGC 2732 (observed by PhP and FS), the receptor was a Tektronix with 512×512 pixels of $0.78''$; the seeing was $2.6''$. For all three objects, standard processing was applied, and calibration was achieved by comparison to standard galaxies. Isophote maps are presented in Fig. 1.

Accurate determination of the PSF was made by fitting two gaussian components to stellar images close to the galaxies.

For NGC 4111, an asymmetry of the photometric profiles along the opposite semi-minor axes was noted by Michard & Simien (1993), who interpreted it as evidence for an extended layer of absorbing material within the equatorial plane (this should also be an indication that the angle of inclination is not exactly $90°$). To bypass this complication, we have symmetrized the brightness distribution, adopting the brightest side which is, presumably, farther away from the observer (and hence less absorbed).

Since our discussion on mass-to-light ratios will involve color gradients, we also present in Fig. 2 the $(U-V)$ and $(V-I)$ profiles along the main axes, from unpublished observations by one of us (RM), obtained at the same telescope as the V frames.

2.3. Long-slit spectroscopy

Absorption spectra were obtained at the CARELEC spectrograph attached to the 1.93-m telescope at OHP. For NGC 4111 and N4350 (observed by RM), we have used the data already

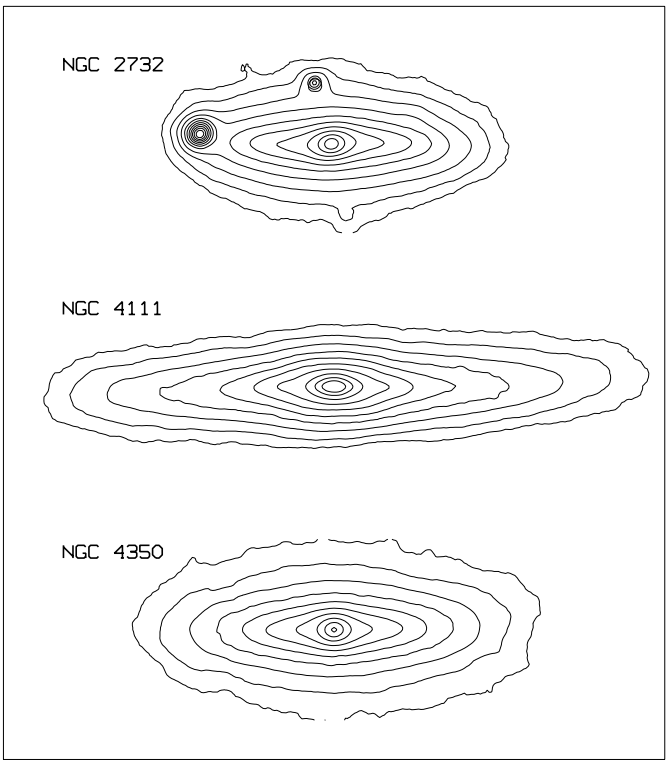

Fig. 1. Isophote maps for the three objects. The box is $4'$ wide. The innermost contour is $\mu_V = 16.75$, and the step is 0.75 mag arcsec^{-2}. For NGC 4111, a twist of the outermost isophotes is visible

presented in Simien at al. (1997c), but reprocessed with an improved Fourier-Fitting algorithm. For these observations, since the exact star-image dimensions are unfortunately unavailable, we have adopted an average seeing disk of $3''$ FWHM. For NGC 2732, we have used the kinematic profiles in Simien & Prugniel (1997a) for the inner region (seeing $2.5''$), and those in Simien & Prugniel (1997c) for the outer regions (seeing $\simeq 4''$).

For comparison, we also included kinematic measurements from other sources: Seifert & Scorza (1996; hereafter SS96) for the three galaxies and, for NGC 4111 and NGC 4350, Fisher (1997; hereafter F97). A few data on the instrumental settings are presented in Table 2. No information on the seeing conditions are given by these papers; in Sect. 4, as a working hypothesis, we will assume a value of $1.5''$ for F97. Besides rotation-velocity and velocity-dispersion profiles (V and σ), F97 presents the h_3 and h_4 shape parameters of the line-of-sight velocity distribution (LOSVD), for the inner regions; for our purpose, however, we make use of the "classical" profiles; it is worth mentioning that these were determined independently of the h_3 and h_4 parameters, with a conventional Fourier technique.

The case of the minor axis of NGC 4111 is particular. Close inspection of the kinematic data of F97 shows that the major-axis profiles have a symmetry center slightly off the position $r = 0$; moreover, the minor-axis rotation is significantly variable, and set to $V = 0$ for $r = 0$. We believe this provides evidence that the minor-axis spectrum was off-centered by roughly $0.4''$ (half a pixel): for this, the F97 velocities were shifted by 30 km s^{-1},

Table 2. Instrumental settings for spectroscopy

	Seifert & Scorza (1996)	Fisher (1997)	This work
Spectral range (Å)	4700-5600	4215-5617	4835-5735[a] / 5060-5510[b]
Pixel size (Å× arcsec)	1.1×0.9	3.1×0.8	1.8×1.2[a] / 0.9×1.2[b]
Slit width (arcsec)	3.0	2.0	2.2[a] / 2.1[b]

Notes. [a] NGC 2732; [b] NGC 4111 and NGC 4350.

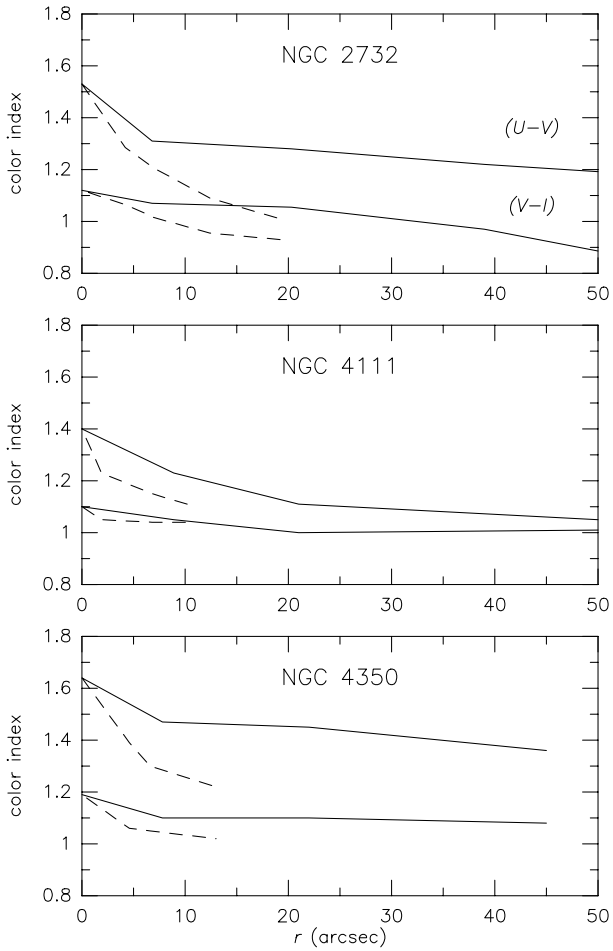

Fig. 2. Color gradients along the main axes. Profiles of color indices, corrected for Galactic extinction, are displayed along the major axis (*solid lines*) and the minor axis (*dashed lines*)

and (Sect. 4) our model was calculated along an axis situated at that distance from the actual minor axis.

Although not everywhere in perfect coincidence, the kinematic data from the three sources have been combined, and used for the model fit (Figs. 4, 5, and 6).

3. Space density of luminosity and mass

The MGE method requires the fitting of the observed surface-brightness distribution by a sum of gaussian components; since our galaxies show no evidence for large isophotal twists, and little evidence for strong asymmetries (except NGC 4111 before symmetrization), we assigned the same values to the center coordinates and orientation for all components of the same object. We selected an isophote of semi-major axis r between 50 and $80''$ as the appropriate outer boundary for the fitting; we used a χ^2-minimization routine to determine, for each gaussian, the characteristic radius s, the central brightness I_0 (or μ_0 in magnitude scale), and the apparent ellipticity ϵ; we started with two components, adding up an additional one after each convergence, until a satisfactory result was reached.

The MGE method allows a straightforward deconvolution by a single-gaussian PSF; in our case, however, we have two-gaussian PSFs with (in the worst cases) a width close to that of the innermost component, and we found that the fitting with gaussian components already convolved by the PSF was the more reliable technique.

Table 3 presents the result of the model representation with gaussian components. It is interesting to note that a very limited number of these provides a satisfactory fit (in terms of "$O-C$" residuals) within the range needed for the kinematic modeling. Although each component lacks physical significance, the outward variation of the s, μ_0, and ϵ parameters for a given galaxy adequately reflects the transition between a central, steep bulge and a larger, shallower, and highly flattened disk.

The flattest of the three objects, NGC 4111, deserves a particular comment: the complex inner structure of this object has already been noted by, e.g., SS96 and F97, who show evidence for a nuclear disk within $\simeq 6''$ from the center; our compact ($s = 3.5''$) and highly flattened ($\epsilon = 0.72$) component #2 is a confirmation.

The derived gaussian components can easily be converted to 3D density distributions, once an inclination angle is fixed; for the present purpose, ignoring the telltale asymmetry of NGC 4111, we assume that the galaxies are edge-on. Then, assigning a mass-to-light ratio ($\mathcal{M}/L$) to each component fully determines the mass distribution.

4. Modeling the kinematics

4.1. The 'basic' dynamical model

Let us consider a collisionless, axisymmetric galaxy and cylindrical (r, θ, z) coordinates. We assume that the system is stationary and has a distribution function of the type $f(E, L_z)$, i.e. depending on the energy and the angular momentum along the rotation axis. Then, the classical second-order Jeans equations (e.g., Binney & Tremaine 1987) connect the following parameters: a) the density of mass and the gradients of the potential, and b) the first- and second-order kinematic moments; these

Table 3. Multi-Gaussian fitting to the observed luminosity distribution

	NGC 2732				NGC 4111				NGC 4350			
Parameters:	#	s	μ_0	ϵ	#	s	μ_0	ϵ	#	s	μ_0	ϵ
	1	0.63	15.76	0.24	1	1.34	16.07	0.50	1	0.73	16.19	0.10
	2	2.15	17.58	0.27	2	3.48	16.32	0.72	2	2.23	17.09	0.22
	3	4.60	18.53	0.34	3	3.66	17.32	0.35	3	4.92	18.84	0.24
	4	17.27	19.50	0.83	4	11.47	18.59	0.53	4	15.12	18.89	0.78
	5	23.06	20.41	0.66	5	21.38	19.37	0.87	5	29.27	20.21	0.67
					6	52.71	20.60	0.84				
Residuals:		r	$\delta\mu(r)$			r	$\delta\mu(r)$			r	$\delta\mu(r)$	
		20	0.07			20	0.03			20	0.02	
		50	0.08			80	0.13			70	0.08	
						100	0.22					

Notes. Parameters: component number (#), characteristic radius (s) in arcsec, central brightness (μ_0) in V mag arcsec^{-2}, and apparent ellipticity (ϵ). Residuals: rms residual $\delta\mu(r)$, in mag arcsec^{-2}, between the multi-component model and the observed luminosity, within an ellipse of semi-major axis r, in arcsec (the flattening of this ellipse is selected close to that of the local isophote).

are the mean rotational velocity ($\overline{\Theta}$), and the residual-velocity dispersion (through its components σ_r, σ_θ, and $\sigma_z \equiv \sigma_r$).

With the MGE density representation, calculation of the potential derivatives is straightforward at any (r, z) point in the galaxy (Emsellem et al. 1994a).

Next, making a choice between isotropy and anisotropy and, in the latter case, adopting a specific form of the velocity ellipsoid, fully determines the local $\overline{\Theta}$ and the σ components by simple numerical integrations. Then, an approximation to the actually observed rotation V and dispersion σ can be derived by projecting the luminosity-weighted quantities along the line of sight.

The result allows accurate comparisons to spectroscopic data under two conditions: the local velocity distribution (VD) is very close to a gaussian, and the luminosity-weighted projection of the VDs along the line of sight (LOSVD) is also very close to a gaussian. But, for elliptical galaxies, dynamical models do not always return gaussian VDs (e.g., Magorrian & Binney 1994: hereafter MB94; Evans 1994); and the spectra of many early-type galaxies do show non-gaussian LOSVDs (e.g., van der Marel & Franx 1993; Bender et al. 1994; F97). Flattened S0s, featuring a hot central component and a colder, rapidly rotating disk, are amongst the objects with the most strongly non-gaussian LOSVDs.

For the model calculations, higher-order Jeans equations can be derived (MB94), which involve higher-order moments defining the exact shape of the VDs. And expansion of the LOSVD into Gauss-Hermite polynomials (van der Marel & Franx 1993; MB94) can quantify its departure from the pure gaussian shape. This powerful method, however, adds significant complexity to the model fitting. It can be applied only to the limited radial range where the S/N ratio of the spectra allows a reliable recovery of the high-order terms in the LOSVD representation.

For our edge-on S0s, we adopt a simplified model relying on the following hypotheses: for each component, the shape of its individual VD within the combined potential is gaussian and isotropic, so that it is determined by the second-order Jeans equations[1]. So, locally, the global VD is mainly determined

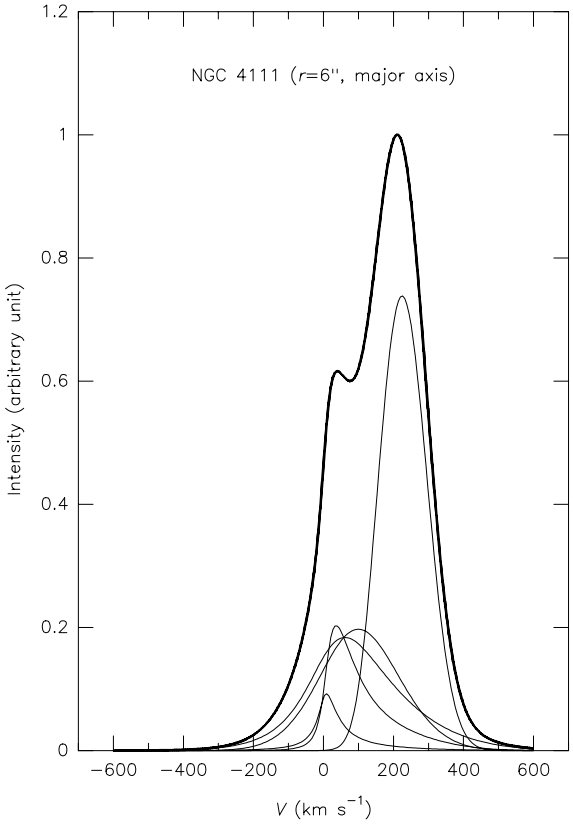

Fig. 3. An example of the LOSVD derived from the basic model for NGC 4111 (with the same $\mathcal{M}/L$ ratio for all components), at $6''$ from the center along the major axis. The contribution of individual components (*thin lines*) are shown, as well as the resultant (*thick line*). At this particular point of the galaxy, the dominant contribution is from the flattened component #2; the negligible contribution of component #1 is not visible

[1] Strict isotropy assumed for a roundish component within a flatter potential can lead to negative values of $\Theta^2_{\rm m}$; this, however, occurs at low

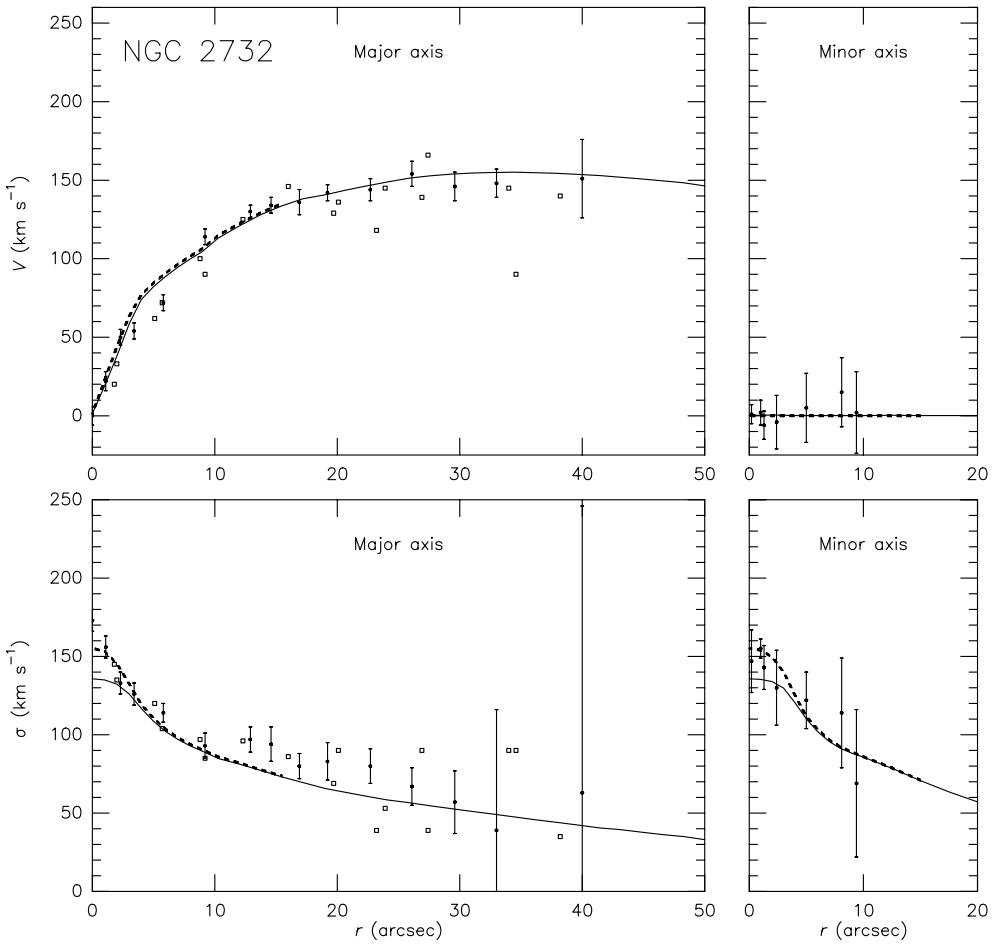

Fig. 4. The kinematics of NGC 2732. Rotation (V) and dispersion (σ) profiles along the main axes. *Filled dots and error bars*: this work (see Sect. 2.3); *open squares*: SS96 (Seifert & Scorza 1996); *solid line*: model of Sect. 4.1, with $\mathcal{M}/L = 3.6$ for all components; *dashed line*: same model, incorporating an additional central mass of $5 \times 10^8 \mathcal{M}_\odot$

by the difference in flattening and central concentration of the components, which implies significantly different rotation velocities; as a consequence, this can adequately represent strongly non-gaussian LOSVDs, and Fig. 3 gives an example. For each galaxy, we have adopted the following process:

- for a selected line of sight S, we defined a series of points P_i along this line; at each P_i, we solved the second-order Jeans equations for each component, and we calculated the local, resulting VD;
- we averaged the VDs along the line of sight to get the LOSVD at S;
- we convolved the LOSVDs from neighboring points on the plane of the sky, to simulate the seeing effects during the spectroscopic observations, and we binned according to the slit width and pixel size;
- we then convolved a K-giant spectrum by this final LOSVD, and ran our Fourier-Fitting program on the resulting spectrum, to get the V and σ values at position S.
- the above sequence was repeated for several points along the main axes.

densities, in the outer regions of the component where its luminosity is very low: the contamination of the LOSVD due to this anomaly can thus be overlooked.

This provided us with rotation-velocity and velocity-dispersion profiles directly comparable to the results of observations reduced with a "classical" algorithm, i.e., assuming implicitly a gaussian velocity profile.

We began with a basic model characterized by the same value of the $\mathcal{M}/L$ ratio for all components, adjusted to provide the best overall fit. Figs. 4, 5, and 6 show the fit to the observations. The $\mathcal{M}/L$ ratios are listed in col. (2) of Table 4.

Except for the very center, the global agreement is satisfactory. For all three galaxies, there is an obvious discrepancy in the innermost region, especially for the velocity dispersion; to correct for this, several solutions are available, which we are going to examine in turn: a) the presence of an added central mass, b) an increase of the inner $\mathcal{M}/L$, or c) an ad hoc anisotropy of the residual velocities.

4.2. Additional central mass

The possibility of a central point mass has an attractive characteristic: with respect to the basic model, it involves only one additional free parameter. Figs. 4, 5, and 6 also show the fit for the resulting models, incorporating masses adjusted to improve mainly the value of the central velocity dispersion, σ_0. These masses are listed in col. (4) of Table 4. We note that they repre-

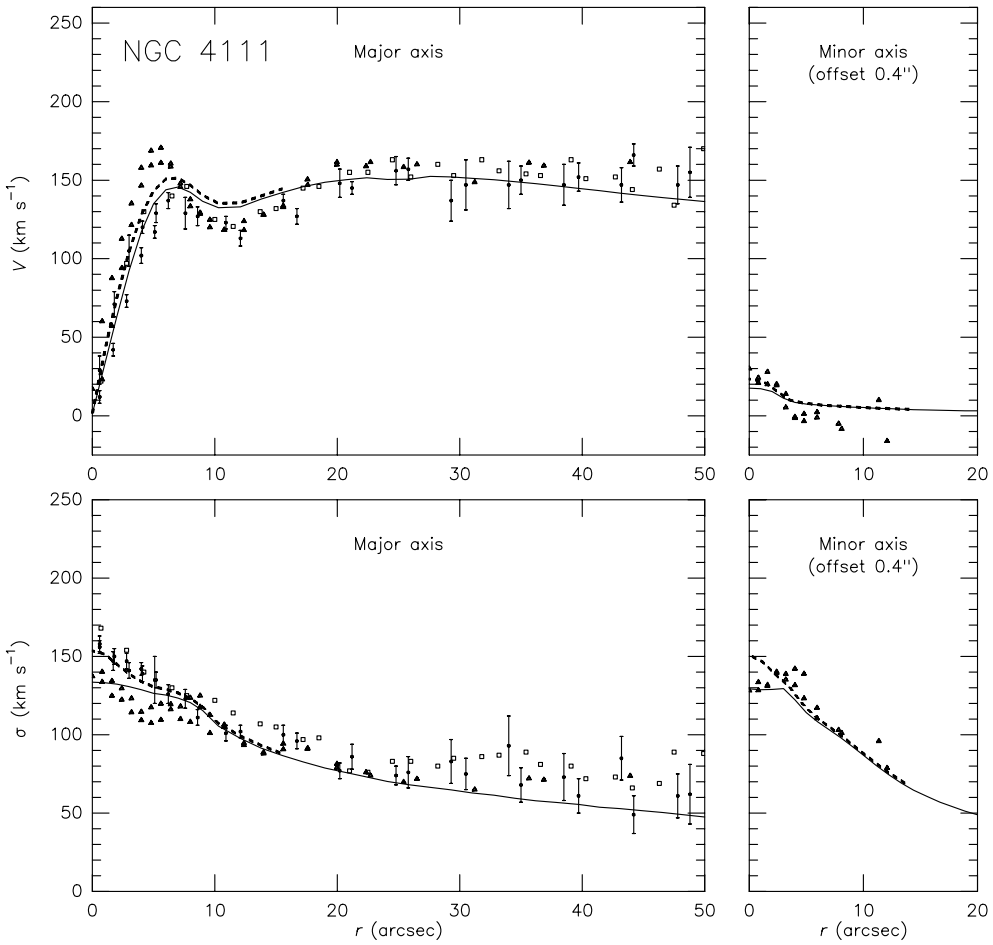

Fig. 5. The kinematics of NGC 4111. Same symbols as in Fig. 4. In addition, *filled triangles*: F97 (Fisher 1997). $\mathcal{M}/L = 4.0$

sent between 1 and 1.5% of the total mass of the galaxies, and roughly half the mass of the innermost component.

4.3. Variation of the central stellar $\mathcal{M}/L$ ratio

Another way to derive a higher σ_0 is to assume an increase of the stellar $\mathcal{M}/L$ ratio close to the nucleus, a variation in qualitative agreement with the observed reddening of the central regions (Fig. 2); the gradients give evidence that the reddening is mostly limited to the inner 5-10″ in radius, and that it likely affects the bulge population. As an experiment, we have gradually increased, inwards, the $\mathcal{M}/L$ of the first three components (those mainly representative of the bulge), so that the new σ_0 is roughly the same as for the point mass.

For components #1, 2, and 3, respectively, we adopted $\mathcal{M}/L$ values of: 5.3, 4.0, and 3.6 (NGC 2732); 7.3, 4.3, and 4.3 (NGC 4111); and 11.5, 8.0, and 7.0 (NGC 4350).

For each galaxy, the global mass difference is listed in col. (5) of Table 4. Expectedly, the mass increase is higher than than with a point mass; it now represents between 3 and 5% of the mass of the galaxy. The kinematic profiles obtained are discussed in Sect. 5.

4.4. Anisotropy?

Let us relax the $f(E, L_z)$ assumption momentarily, so that any geometry of the velocity ellipsoid can be considered. Then, it is well-known that a radial anisotropy in the central region is efficient in enhancing σ with respect to V; but, for obvious reasons of symmetry, isotropy must hold at the very center. Far from the center, a radial anisotropy would have the opposite effect: it would lower σ with respect to V, making things worse. In contrast, a tangential anisotropy would increase the discrepancy near the center. So, the variation of the degree of anisotropy, if any, is likely a complicated function of r and z on which the constraints are marginal with the present data.

For these reasons, we consider that any anisotropy is beyond the scope of this preliminary study.

5. Discussion

5.1. Global kinematics

We have seen that our model kinematics fit the intermediate regions of the galaxies satisfactorily. Several features of the rotation curves, for which SS96 presented qualitative interpretations, are accounted for by the actual mass distribution and by the reduction characteristics.

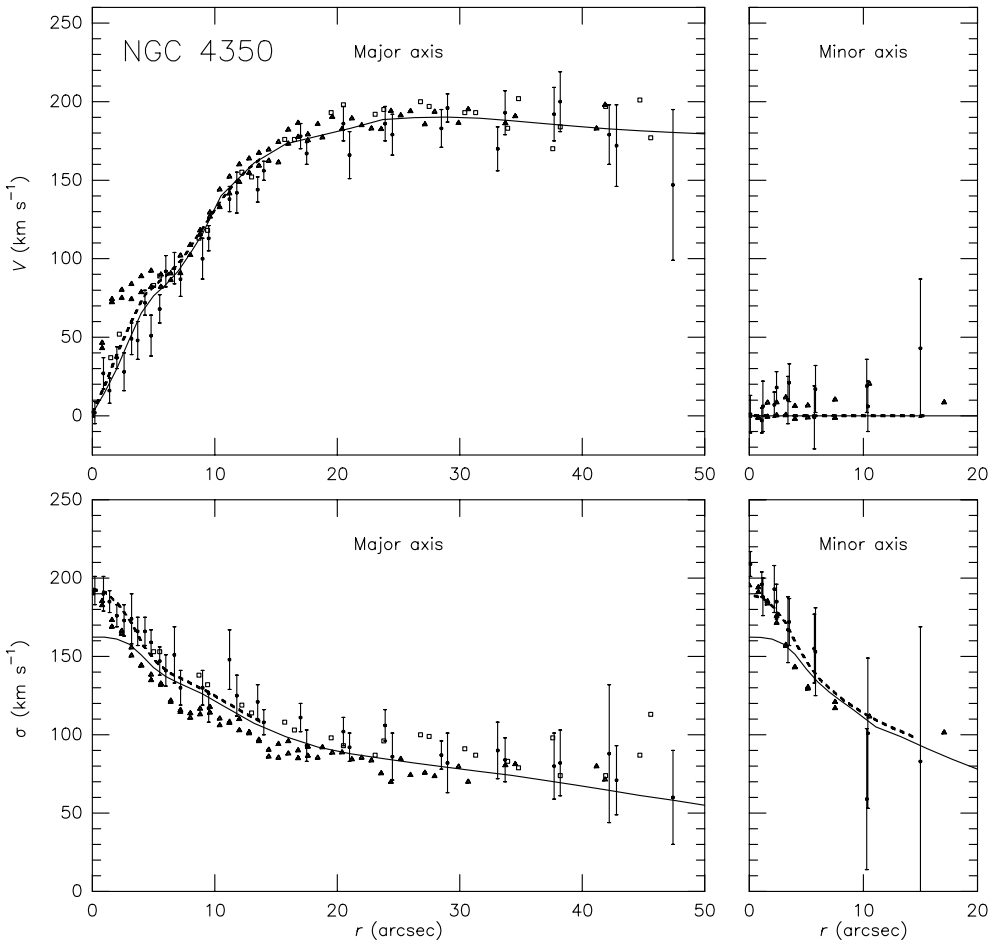

Fig. 6. The kinematics of NGC 4350. Same symbols as in Fig. 4 and Fig. 5. *solid line*: model of Sect. 4.1, with $\mathcal{M}/L = 7.0$ for all components; *dashed line*: same model, incorporating an additional central mass of $6 \times 10^8 \mathcal{M}_\odot$

Table 4. Derived masses and $\mathcal{M}/L$ ratios

Object	$\mathcal{M}/L$	$\mathcal{M}_{\rm total}$	$\Delta\mathcal{M}_{\rm central}$	$\Delta\mathcal{M}_{\rm stellar}$
(1)	(2)	(3)	(4)	(5)
NGC 2732	3.6	0.48×10^{11}	0.50×10^9	1.70×10^9
NGC 4111	4.0	0.30×10^{11}	0.50×10^9	1.50×10^9
NGC 4350	7.0	0.57×10^{11}	0.80×10^9	2.10×10^9

Notes. Col. (2): $\mathcal{M}/L$, V-band mass-to-light ratio for the basic model (Sect. 4.1), in solar units; col. (3): $\mathcal{M}_{\rm total}$, integrated mass of the galaxy, in $\mathcal{M}_\odot$, for a constant $\mathcal{M}/L$ from col. (2); col. (4): $\Delta\mathcal{M}_{\rm central}$, additional central point mass needed to improve the fit in the inner regions (Sect. 4.2); col. (5): $\Delta\mathcal{M}_{\rm stellar}$, additional mass from an increase of the stellar mass-to-light ratio in the central region, giving the same central velocity dispersion as the point mass (Sect. 4.3).

Our data do not reach radii where evidence is seen for dark matter. It appears that the rotation of the disks provide the tightest constraint on the $\mathcal{M}/L$s. We note that the calculated rotation is marginally too high with respect to the dispersion; this reflects the "reluctance" of our models to consider a non-edge-on inclination (a smaller inclination would flatten the components and further increase the rotation); actually, for a 5° tilt, the change in the $\mathcal{M}/L$ values is between 3% (NGC 4350), and 20% (NGC 4111).

The scatter in our three $\mathcal{M}/L$ values is no larger than what it is expected from the uncertainty on the redshift distances. The average value is consistent with another edge-on S0, NGC 3115 (of comparable absolute magnitude), for which Capaccioli et al. (1993) found $\mathcal{M}/L_B = 6$ in the central region.

5.2. Central masses

To resolve the discrepancy at the center, we have considered the effect of an additional point mass. Given the resolution of our data, the constraints on this mass are not very tight; however, our results (from 0.5 to $0.8 \times 10^9 \mathcal{M}_\odot$) are bracketed by two other cases, for which high-resolution and HST observations have led to the following results: a) in the E5 galaxy NGC 3377, a massive black hole with a mass in the range from 0.05 to $0.2 \times 10^9 \mathcal{M}_\odot$ (Richstone et al. 1996); b) in NGC 3115, a supermassive black hole of $2 \times 10^9 \mathcal{M}_\odot$ (Kormendy at al. 1996).

The alternative solution, the $\mathcal{M}/L$ variation, obviously involves more arbitrariness; the basic model is compared to this solution and to the point mass in Fig. 7, which presents a close-up of the inner $15''$ along the major axis. Not unexpectedly, our data do not allow a clear-cut discrimination, although there is marginal evidence that the point-mass solution would be a better fit; this, however, is quite sensitive to the adopted seeing condition for the spectroscopic observations.

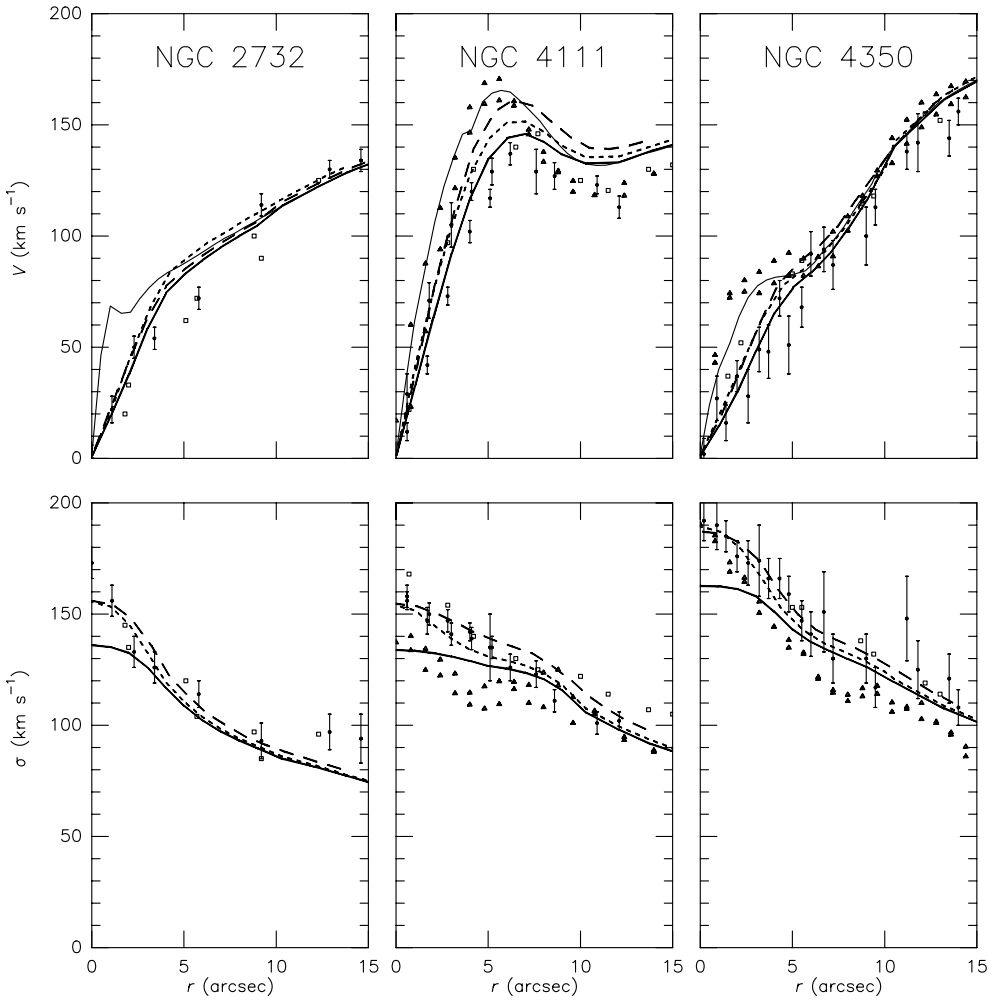

Fig. 7. The kinematics of the major-axis inner regions. The data from the same sources as in Figs. 4, 5, and 6 are displayed together with several model curves. *Thick solid lines*: basic model; *short-dashed lines*: same model incorporating a central mass (Sect. 4.2 and Table 4); *long-dashed lines*: model with a $\mathcal{M}/L$ variation (Sect. 4.3). In addition, for the V profiles, *thin solid lines*: the raw basic model, i.e., unconvolved for seeing effects or instrumental resolution

For comparison, Fig. 7 also shows the rotation of the unconvolved basic model. We note that, where the F97 data depart significantly from the other two sources, the unconvolved model provides a better fit. This may be a consequence of the uncertainties on the spectroscopic resolution effects.

How much are our results dependent on the photometric resolution? In the inner regions of several other S0 galaxies at comparable distances, HST photometric profiles (Lauer et al. 1995) show, quite expectedly, gradients dramatically steeper than those of our innermost gaussians; therefore, are our PSF-deconvolved components accurate enough for our purpose? We performed tests which showed that the additional mass needed to improve the kinematic fit, when spread uniformly throughout component #1, is found between 50 and 90% higher that when supposed point-like; these are certainly upper limits to the errors on the mass due to the resolution, and the actual errors are probably significantly lower, given the fair accuracy of our PSFs. Although this contributes to the ambiguity between point-mass and stellar-$\mathcal{M}/L$ effects, the overall mass distribution is no more than marginally affected.

5.3. Stellar populations

Let us go back to the question of the $\mathcal{M}/L$ variation. It would be interesting to find a link between the $\mathcal{M}/L$ increase and the color gradients, with the help of a stellar-population model. For this, we first remark that the central increase of $(U-V)$ is $\approx$ 0.2-0.3 mag, and that of $(V-I)$ is $\approx$ 0.1-0.2; these are lower limits, since no correction has been applied to compensate for the effect of the integration along the line of sight. We now look at the models of Worthey (1994), who lists in his Table 5A several $\mathcal{M}/L$s and color indices for a range in age and metallicity; although derived for a homogeneous, single-burst population, these data are helpful here, since they provide a relation between color and $\mathcal{M}/L$ ratio[2]. Averaging the data for ages of 8 and 12 Gyr (corresponding to $\mathcal{M}/L_V$ of 4.5 and 6.3, respectively), we note that for [Fe/H] between the acceptable

[2] On a sample of S0s, Fisher et al. (1996) have investigated the relation between the $(B-R_C)$ color index and the Mg_2 metallicity index. They found that for most objects (including NGC 4350), the Worthey models are compatibles with the observed relation; one of the exceptions is the inner region of NGC 4111, probably because of the reddening due to the dust (our symmetrization, however, may have limited the consequences of this).

limits of -0.25 and $+0.25$, $(U-V)$ increases by ≈ 0.5 and $(V-I)$ by ≈ 0.2, and that $\mathcal{M}/L_V$ increases by $\approx 35\%$. This value is to be compared to our inward increase of $\mathcal{M}/L$, which is $\approx$ 50, 80, and 60% for NGC 2732, NGC 4111, and NGC 4350, respectively. To sum up, with respect to the model, we find $\mathcal{M}/L$s of the same order, but increasing too much towards the center; given the uncertainty on the distances, on the one hand, and the crudeness of our color-index handling, on the other hand, there is no apparent incompatibility.

Most current models of stellar population fail to predict all the characteristics of actual galaxies, and it is well-known that contradictions do exist between competing works (Buzzoni 1995a; Silva 1996). Obviously, other models (e.g., Buzzoni 1989, cw1995b; Bruzual & Charlot 1993; Vazdekis et al. 1996) should also be considered in a study more exhaustive than the present one; for objects with well-determined distances, edge-on galaxies could provide convenient tests for comparing these different models, especially when the metallicity-index profiles are also available.

6. Conclusion

We have calculated the mass distribution for three edge-on S0 galaxies. Our aim was to investigate what applications could be considered with the data used, and to provide a basis for the subsequent improvement in both analysis and observational material. Our results can be summarized as follows:

- Photometric and spectroscopic data of average resolution (and lower than average, for some of them), together with the MGE technique and an "inexpensive" model, are able to reproduce the observed major- and minor-axis kinematics, in a range encompassing a large fraction of the visible mass. This represents a fair level of constraints on possible models, and this can be extended to many other galaxies for which data is already available.
- The flexibility of the visible-mass representation, and its moderate model dependency, can easily be used to test dark-matter content, if deeper kinematics are available.
- The derived $\mathcal{M}/L$ ratios can be used for testing stellar-population models. And with a goal obviously more limited than that permitted by high spatial resolution (e.g. the center of M104: Emsellem et al. 1996), we have seen that a few issues on the inner population gradients are probably at hand; this, among other applications, could contribute to tighten the constraints on the mass of an hypothetical central object.

Acknowledgements. We are pleased to thank E. Emsellem, G. Galletta, and E. Pignatelli for interesting discussions. We have made use of the Lyon-Meudon Extragalactic Database operated by the LEDA team.

References

Bender, R., Saglia, R. P., Gerhard, O. E. 1994, MNRAS 269 785
Binney, J., Tremaine, S. 1987, Galactic Dynamics, Princeton Univ. Press
Bruzual A., G., Charlot, S. 1993 ApJ 405, 538
Buzzoni, A. 1989, ApJS 71, 817
Buzzoni, A. 1995a, in: Fresh views of elliptical galaxies, Buzzoni, A., Renzini, A., Serrano, A. (eds.), ASPCS, vol. 86, 189
Buzzoni, A. 1995b, ApJ 98, 69
Capaccioli, M., Held, E. V., Nieto, J.-L. 1987, AJ 94, 151
Capaccioli, M., Cappellaro, E., Held, E. V., Vietri, M. 1993, A&A 274, 69
de Vaucouleurs, G., de Vaucouleurs, A., Corwin, H. G. jr., Buta, R. J., Paturel, G., et al. 1991, Third Reference Catalogue of Bright Galaxies, Springer-Verlag (New-York) (RC3)
Emsellem, E., Monnet, G., Bacon, R. 1994a, A&A 285, 723
Emsellem, E., Monnet, G., Bacon, R. 1994b, A&A 285, 739
Emsellem, E., Bacon, R., Monnet, G., Poulain, P. 1996, A&A 312, 777
Evans, N. W. 1994, MNRAS 267, 333
Fisher, D. 1997, AJ 113, 950 (F97)
Fisher, D., Franx, M., Illingworth, G. 1996, ApJ 459, 110
Kormendy, J., Bender, R., Richstone, D., Ajhar, E. A., Dressler, A., et al. 1996, ApJ 459, L57
Lauer, T. R., Ajhar, E. A., Byun, Y.-I., Dressler, A., Faber, S. M., et al. 1995, AJ 110, 2622
Lucy, L. B. 1974, AJ 79, 745
Magorrian, S. J., Binney, J. 1994, MNRAS 271, 949 (MB94)
Michard, R., Simien, F. 1993, A&A 274, L25
Monnet, G., Bacon, R., Emsellem, E. 1992, A&A 253, 366
Richstone, D., Gebhardt, K., Kormendy, J., Bender, R., Magorrian, J., et al. 1996, BAAS vol. 189, #111.02
Seifert, W., Scorza, C. 1996, A&A 310, 75 (SS96)
Scorza, C., Bender, R. 1990, A&A 235, 49
Scorza, C., Bender, R. 1995, A&A 293, 20
Sérsic, J.-L. 1968, AJ 73, 892
Silva, D. R., 1996, in: Spiral galaxies in the near IR, Minniti, D., Rix, H.-W. (eds.), Springer (Berlin), p. 3
Simien, F., Michard, R. 1990, A&A 227, 11
Simien, F., Prugniel, Ph. 1997a, A&AS 122, 521
Simien, F., Michard, R., Prugniel, Ph. 1993, in: Structure, dynamics, and chemical evolution of elliptical galaxies, Danziger, I. J., Zeilinger, W. W., Kjaer, K. (eds.), ESO Conference and Workshop Proceedings, vol. 45, 211
van der Marel, R. P., Franx, M. 1993, ApJ 407, 525
Vazdekis, A., Casuso, E., Peletier, R. F., Beckman, J. E. 1996, ApJS 106, 307
Worthey, G. 1994, ApJS 95, 107